Comparison of Navier-Stokes simulations with long-wave theory: Study of wetting and dewetting

K. Mahady, S. Afkhami, J. Diez, and L. Kondic

Citation: Physics of Fluids (1994-present) **25**, 112103 (2013); doi: 10.1063/1.4828721

View online: http://dx.doi.org/10.1063/1.4828721

View Table of Contents: http://scitation.aip.org/content/aip/journal/pof2/25/11?ver=pdfcov

Published by the AIP Publishing

PHYSICS OF FLUIDS **25**, 112103 (2013)

Comparison of Navier-Stokes simulations with long-wave theory: Study of wetting and dewetting

K. Mahady,[1] S. Afkhami,[1] J. Diez,[2] and L. Kondic[1]
[1]*Department of Mathematical Sciences, New Jersey Institute of Technology, Newark, New Jersey 07102, USA*
[2]*Instituto de Fisica Arroyo Seco (CIFICEN-CONICET), Universidad Nacional del Centro de la Provincia de Buenos Aires, Pinto 399, 7000 Tandil, Argentina*

(Received 26 March 2013; accepted 10 October 2013; published online 7 November 2013)

The classical long-wave theory (also known as lubrication approximation) applied to fluid spreading or retracting on a solid substrate is derived under a set of assumptions, typically including small slopes and negligible inertial effects. In this work, we compare the results obtained by using the long-wave model and by simulating directly the full two-phase Navier-Stokes equations employing a volume-of-fluid method. In order to isolate the influence of the small slope assumption inherent in the long-wave theory, we present a quantitative comparison between the two methods in the regime where inertial effects and the influence of gas phase are negligible. The flow geometries that we consider include wetting and dewetting drops within a broad range of equilibrium contact angles in planar and axisymmetric geometries, as well as liquid rings. For perfectly wetting spreading drops we find good quantitative agreement between the models, with both of them following rather closely Tanner's law. For partially wetting drops, while in general we find good agreement between the two models for small equilibrium contact angles, we also uncover differences which are particularly evident in the initial stages of evolution, for retracting drops, and when additional azimuthal curvature is considered. The contracting rings are also found to evolve differently for the two models, with the main difference being that the evolution occurs on the faster time scale when the long-wave model is considered, although the ring shapes are very similar between the two models. © *2013 AIP Publishing LLC*. [http://dx.doi.org/10.1063/1.4828721]

I. INTRODUCTION

Wetting and dewetting phenomena involve the displacement of two immiscible fluids in contact with a solid surface. This problem has been extensively studied both theoretically and experimentally (see, e.g., Refs. 1–8 for a review). Simulating such phenomena is complicated, in part, by the presence of the fluid-fluid interface whose evolution must be computed as a part of the solution of the governing equations. One approach to deal with these complexities is to formulate the problem within the long-wave (L-W, lubrication) theory that assumes small slopes everywhere, and in addition is typically derived assuming negligible inertial effects. The L-W approach allows the reduction of the complicated mathematical description to a simpler problem of a nonlinear 4th order partial differential equation for the fluid thickness.

Due to its (relative) simplicity, the L-W approach has been extensively used to model wetting and dewetting phenomena, see Refs. 9 and 10 for reviews. Often, this approach has been implemented to consider experimental configurations where contact angles are not necessarily small. This extension of the use of the L-W model outside of its strict range of validity has been in part justified by comparing the solution profiles close to the contact lines between the L-W model and the solutions of Stokes equations,[11] with only relatively minor differences found. While this is encouraging, we are unaware of benchmark tests considering the validity of L-W model by comparing its solutions to direct numerical solutions of the full Navier-Stokes (N-S) system in a fully dynamic setting. One

example of a problem where such tests are crucial is the evolution of liquid metals on nanoscale due to large contact angles involved. In Ref. 12, for example, liquid nickel was considered on SiO_2 substrate, where contact angle is close to $\pi/2$, and therefore the use of the L-W theory is questionable. To accurately describe the evolution under the given conditions, it is important to consider a more complete theory, and discuss the degree of agreement. This agreement (or lack of it) is of relevance also for practical reasons: obtaining direct solutions of N-S equations is computationally demanding, and knowing precisely when L-W model can be used, and with which degree of accuracy, is needed.

The comparison between the results of N-S equations and the long-wave model is the main focus of this paper. As will be discussed in detail, carrying out this comparison in a meaningful way is not trivial, since the models necessarily involve their own sets of definitions of relevant quantities (such as contact angle). Therefore, comparing "raw" data, such as front positions as a function of time, for example, turns out not to be always very insightful; instead, we carry out the comparison by considering the degree of agreement of the two models with asymptotic solutions in the form of Cox-Voinov (C-V)[13] and Tanner's laws[14] for the flow regimes where these laws are expected to be valid. To facilitate the comparison between the models and the asymptotic solutions, we concentrate on flow configurations such that inertial effects are not significant (to the degree possible), capillary numbers are reasonably small, and the effect of the gas phase is minimal. Furthermore, we consider relatively simple flow geometries, so to be able to focus on the comparison between the models, and not necessarily on the complexities which may be expected if more complicated flow problems were treated. First, we consider the classical problem of a wetting or dewetting drop on a substrate in two and three dimensions. Second, motivated by recent works on liquid metals,[15–17] we investigate the fluid ring geometry.[18]

The remainder of this paper is organized as follows. In Sec. II, we present the full governing equations including a Navier slip model[19–22] to alleviate the stress singularity at the moving contact line which occurs when the no-slip condition is applied on the substrate.[23] Some details of the volume-of-fluid (VoF) based numerical solver are given in Appendix A, followed in Appendix B by a convergence study as well as a comparison with the asymptotic result[21] of Hocking-Rivers. We continue by describing the L-W model which also uses the slip model for consistency with the VoF based solver, and specifies the contact angle via a disjoining pressure approach, discussed in some detail in, e.g., Ref. 24. In Sec. III, we systematically investigate the degree of agreement between the models for both wetting and dewetting problems in two and three (axisymmetric) dimensions. Section IV considers the problem of a fluid ring structure collapsing into a drop. We conclude in Sec. V.

II. MODELS

The governing equations are the incompressible two-phase N-S equations. We will generally refer to one phase of the fluid as the liquid phase, and the other as the gas phase. We nondimensionalize by choosing the velocity scale to be $U = \sigma_0/\mu_\ell$ and the length scale to be $L = \mu_\ell/(\rho_\ell U)$, where ρ_ℓ, μ_ℓ, and σ_0 are the (dimensional) liquid phase density, liquid phase viscosity, and liquid-gas surface tension, respectively. The N-S equations in nondimensional form then become

$$\rho\left(\partial_t \mathbf{u} + \mathbf{u}\cdot\nabla\mathbf{u}\right) = -\nabla p + \nabla\cdot\left[\mu\left(\nabla\mathbf{u} + \nabla\mathbf{u}^T\right)\right] + \sigma\kappa\delta_s\mathbf{n}, \tag{1}$$

$$\nabla\cdot\mathbf{u} = 0. \tag{2}$$

Here, $\rho = 1$ in the liquid phase and $\rho = \rho_g/\rho_\ell$ in the gas phase, where ρ_g is the gas phase density. Similarly, $\mu = 1$ in the liquid phase and $\mu = \mu_g/\mu_\ell$ in the gas phase, where μ_g is the gas phase viscosity. We have σ that represents a unit surface tension. The surface tension force, $\sigma\kappa\delta_s\mathbf{n}$, has been included in Eq. (1) as a body force concentrated at the interface;[25] here, κ is the curvature of the interface between the two fluid phases, δ_s is a delta function centered on the interface, and $\mathbf{n}$ is the unit normal to the interface. The ratios ρ_g/ρ_ℓ and μ_g/μ_{ell} are both set to 1/100; for these ratios, we have found that the influence of the exterior fluid on the results is negligible.

The solution of N-S equations leads to a stress singularity at a moving contact line. Modeling dynamics in this context requires some regularizing scheme to deal with the so-called "contact line singularity," which manifests itself as an infinite stress at the line where the three phases—liquid, gas, and solid—meet. Numerous approaches to overcome this difficulty exist, as reviewed recently in Refs. 8 and 10. In this work, we concentrate on a slip model[19–22] where the no-slip boundary condition at the fluid-solid interface is relaxed. Thus, instead of having vanishing horizontal velocities at the substrate, we assume the Navier slip condition

$$u = \lambda \frac{\partial u}{\partial y}, \tag{3}$$

where the normal to the substrate is in the y direction, the parameter λ is the (nondimensional) slip length, and u is the component of $\mathbf{u}$ tangential to the substrate.

We use Gerris,[26] an open-source solver, implemented in the software package,[27] for the solution of the two-phase N-S equations, in which Eqs. (1) and (2) are solved in an Eulerian frame of reference, and the VoF method is used to track the interface implicitly. Throughout, we will refer to numerical results obtained using Ref. 27 as VoF simulations. An overview of the method, as described in more detail in Ref. 26, as well as the implementation of the contact angle, is given in Appendix A.

A. Long-wave model

The long-wave approach allows for the reduction of the N-S equations to a single nonlinear partial differential equation for the fluid thickness, h. We note that although this approach is strictly valid only for fluid configurations characterized by small free surface slopes, it has been commonly used in partial wetting conditions, i.e., in situations where the contact angle is not necessarily small. The partial wetting conditions can be considered in the model by accounting for van der Waals forces between solid and fluid, as briefly described below.

The comparison between the results of L-W approach and solutions of the Stokes or Navier-Stokes equations has been considered in the literature, but mostly for steady state configurations. For example, Ref. 28 compares the solutions for the steady cross section of a rivulet flowing down a plane obtained by solving the complete N-S equation with the predictions of the L-W approach (see their Table I). For a contact angle of 30°, they find that the differences between both approaches related to the shape of the free surface are of the order of a few percent. The appropriateness of the use of L-W approach was also discussed earlier in Ref. 11. In that work it was shown that there are some differences in the free surface slope between L-W theory and Stokes formulation, but only very close to the contact line.

In the present work, the partial wetting conditions are included in the L-W model via the disjoining pressure $\Pi(h)$, which represents the effects of the intermolecular forces through the solid/liquid interface (see, e.g., Ref. 24 and the references therein). Using the time and length scales defined previously, the resulting (nondimensional) equation for the fluid thickness, $h = h(x, y, t)$,

TABLE I. Values of β resulting from fitting the evolution of planar drops with a spreading law of the form $\theta^3 - \theta_{eq}^3 \propto Ca^{\beta}$, for L-W and VoF simulations.

	VoF	L-W
30°–15°, slip 0.01	0.92	0.89
30°–15°, slip 0.046875	0.96	0.95
45°–30°, slip 0.01	0.98	0.82
45°–30°, slip 0.046875	0.99	0.87
30°–45°, slip 0.01	0.92	1.1
30°–45°, slip 0.046875	0.90	1.2

which also includes the Navier slip boundary condition, Eq. (3), is (see, e.g., Ref. 9)

$$3\,\frac{\partial h}{\partial t} + \nabla \cdot \left(H^3 \nabla \nabla^2 h\right) + \nabla \cdot \left[H^3 \nabla \Pi(h)\right] = 0, \tag{4}$$

where $H^3 = h^2(h + 3\lambda)$. Here, the first term stands for viscous dissipation and the other two terms account for the driving forces, which are surface tension and disjoining pressure, respectively. For disjoining pressure, we use power-law form

$$\Pi(h) = K f(h) = K\left[\left(\frac{h_*}{h}\right)^n - \left(\frac{h_*}{h}\right)^m\right], \tag{5}$$

where the exponents satisfy $n > m > 1$. The first term represents the liquid-solid repulsion, while the second term stands for the attraction, and when they balance, Eq. (5) predicts a stable film of dimensionless thickness $h = h_*$. Here, K is a dimensionless pressure scale given by $K = \mathcal{A}L/(6\pi\sigma_0 h_*^3)$, where $\mathcal{A}$ is the Hamaker constant for the liquid/solid/gas configuration.[29] Instead of characterizing the interaction by means of $\mathcal{A}$, it is also possible to relate K with the equilibrium contact angle, θ_{eq}, as discussed in some detail in, e.g., Ref. 24. Briefly, through the "augmented" Young-Laplace condition, which assumes a local equilibrium of pressures, one obtains $K = \tan^2(\theta_{eq})/(2Mh_*)$, where $M = (n - m)/((m - 1)(n - 1))$; we use $(n, m) = (3, 2)$, and $h_* = 10^{-3}$ except if specified differently. Note that here we are assuming a dependence on θ_{eq} in the form of $(\tan^2\theta_{eq})/2$ instead of $(1 - \cos\theta_{eq})$ as usually seen in the literature.[24,30] In fact, the former dependence comes directly from using the linearized form of the free surface curvature,[31] which is consistent with the hypothesis of small slope in the L-W approximation, while the latter is derived when using the complete (nonlinear) form. The connection between K and θ_{eq} has been recently discussed in more detail in Ref. 32.

In the present work, we concentrate on one-dimensional solutions of Eq. (4), in both planar and axial geometry. To consider both cases simultaneously, we write Eq. (4) in the form

$$3\frac{\partial h}{\partial t} + \frac{1}{x^d}\frac{\partial}{\partial x}\left[x^d H^3 \frac{\partial}{\partial x}\left(\frac{1}{x^d}\frac{\partial}{\partial x}\left(x^d \frac{\partial h}{\partial x}\right) + \Pi(h)\right)\right] = 0, \tag{6}$$

where $d = 0$, 1 for planar and axisymmetric cases, respectively. The evolution from a given initial condition, $h(x, 0)$, towards equilibrium is calculated by solving Eq. (6) using a numerical code discussed elsewhere.[33] It is worth pointing out that inclusion of Navier slip in the present L-W model is not needed from the computational point of view; we include, however, slip effects anyway so to facilitate the comparison with the VoF results, where slip is required. One consequence is the presence of two length scales in the L-W model (the slip length and the thickness of prewetted layer), increasing the complexity. To simplify, we always use $h_* \ll \lambda$ (for $\lambda \neq 0$) so that, as discussed in Sec. III, the results are not influenced by the value given to h_*.

Before proceeding with the comparison of the models, it is worth pointing out their differences: (i) VoF requires externally imposed contact angle, considers a two fluid problem, and includes inertial effects, and (ii) the L-W approach requires the presence of a prewetted layer (of the thickness comparable to h_*), requires disjoining pressure to specify contact angle, and ignores the inertial effects. While, in principle, non-zero contact angle can be implemented in the L-W approach by specifying it externally, we consider on the physical grounds that using disjoining pressure for this purpose is more appropriate. In order to minimize, if not completely remove these differences, in this work we proceed as follows: (i) consider a low inertia, surface tension dominated regime (i.e., the Reynolds and capillary numbers are small); (ii) analyze carefully what is the influence, if any, of the prewetted layer and disjoining pressure on the L-W results; and (iii) concentrate on the ratio of the fluid densities and viscosities in the VoF simulations such that the gas phase has no influence on the results. As we will see below, we find that the influence of the thickness of the prewetted layer and the details of disjoining pressure model are minimal, allowing us to concentrate on the intrinsic differences between the considered models.

III. PARTIALLY WETTING DROPS: SPREADING AND RETRACTING

In the simulations that follow, we take as initial configuration a fluid geometry characterized by an initial contact angle, θ_i, different from the equilibrium contact angle, θ_{eq}, so that the imbalance of forces leads to contact line motion and bulk flow, until θ_{eq} is reached. In particular, we take the initial fluid profile to be the portion of the circle with radius R and center $(0, -R\cos\theta_i)$ lying above the x-axis. In the L-W simulations, the fluid profile is lifted by an amount h_*. An equilibrium contact angle, θ_{eq}, is specified on the solid substrate, and we consider spreading and retracting of planar and axisymmetric drops from the initial to the equilibrium configuration using VoF and L-W simulations.

As we will see below, direct comparison of the two models (e.g., considering front positions as a function of time) suggests significant differences between the two models; the unifying features can be extracted by considering the relation between the instantaneous contact angle, θ, θ_{eq}, and the contact line front velocity, v_f, that is expected to be satisfied based on the well known C-V law[13]

$$\theta^3 - \theta_{eq}^3 = 9Ca \log(h_c/h_m) + O(Ca). \tag{7}$$

Here we define the capillary number as $Ca = \mu_\ell U v_f/\sigma_0$, h_c is a macroscopic length scale, and h_m is a microscopic length scale. With our choice of scales, Ca and the Reynolds number, $Re = \rho_\ell L U v_f/\mu_\ell$, satisfy $Ca = Re = v_f$. Note that the C-V law is derived under the assumptions of Stokes flow dominated by capillary effects, with the only restriction that $\theta < 3\pi/4$.

For our purposes, we consider this general form of the C-V law:

$$\theta^3 - \theta_{eq}^3 = \alpha Ca^\beta, \tag{8}$$

with a prefactor, α, and exponent, β. As we will see, the differences between the two models will require focusing on β when discussing the agreement of the models between themselves, and with this generalized form of the C-V law; α is discussed in some more detail in the Remarks at the end of this section. The exponent β is computed by performing a least squares fit in the above equation over a representative portion of the spreading process, defined by $Ca > 0.001$, and $\theta^3 - \theta_{eq}^3 < 0.7(\theta_i^3 - \theta_{eq}^3)$. This choice ensures that the drop is spreading fast enough so that its speed can be accurately resolved, and removes any transient effects associated with early times. Spreading speeds of the order of or less than 0.01 are typical; this places us in a viscous, capillary regime where the C-V and the L-W equations are applicable. Moreover, this choice ignores the early phase of spreading and retraction, which is not governed by Eq. (8).

For the VoF simulations, the quantities in Eq. (8) are computed in the following way. The front location, x_f, is taken to be the intersection of the reconstructed interface with the x-axis. The front velocity, v_f, is then computed using discrete values of x_f by simple finite differences. Velocities are computed only when the cell which contains the front is of a specified volume fraction; this ensures that the front velocities are all comparable. To find the contact angle, we consider the volumes of the drops. In planar geometry the cross-sectional area is given by $A = R^2(\theta - \sin\theta\cos\theta)$, where R is the radius of the circular cap, while in the axisymmetric case we have $V = (\pi R^3/3)\left(2 - 2\cos\theta - \sin^2\theta\cos\theta\right)$. The front location is given by $x_f = R\sin\theta$, so that fixing the volume V (A in the planar case) yields simple nonlinear equations for the contact angle θ. In the L-W computations, θ is defined as the slope at the inflection point of the thickness profile $h(x, t)$ near the contact region, i.e., where h is close to h_*.

To illustrate the differences between the results of the models, and to further motivate the comparison with the C-V law, Fig. 1 shows $\theta^3 - \theta_{eq}^3$, Ca, and x_f versus time for the planar drop spreading from 30° to 15° with $\lambda = 0.01$. In Fig. 1(a) we see that θ decreases more rapidly in L-W for early times, while for intermediate and large times, the trend in both models is similar, although $\theta^3 - \theta_{eq}^3$ is different in magnitude. The difference in early time behavior is partially explained by the fact that the initial condition, a circular cap, is also the shape of the quasi-static solution for the VoF model, while the L-W drop must relax to its quasi-static shape, which is parabolic (except in the contact line region where it matches smoothly h_*). Another possible reason for the different behavior for early times may be due to the inertial effects that are not included in the L-W model.

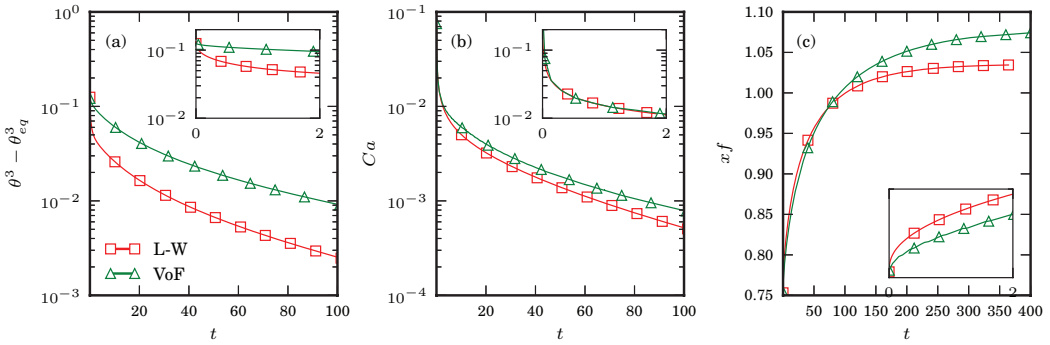

FIG. 1. Planar drop spreading from an initial contact angle of 30° to an equilibrium contact angle of 15°, with $\lambda = 0.01$ for L-W and VoF simulations, showing, as a function of time: (a) $\theta^3 - \theta^3_{eq}$, (b) capillary number Ca, and (c) front location x_f. Note different time range in the part (c). Insets plot each quantity for $t < 2$.

The inset in Fig. 1(b) shows that the behavior of Ca is similar in both models for early times, and although Ca is somewhat smaller for the L-W model, both evolutions share similar trends. Figure 1(c) shows the front location as a function of time. As mentioned above, the final equilibrium shapes are different for L-W and VoF, and consequently, their equilibrium values of x_f differ as well.

In order to compare the results with the C-V law, we consider three cases: a small contact angle drop spreading from $\theta_i = 30°$ to $\theta_{eq} = 15°$ already considered in Fig. 1; a larger contact angle drop spreading from $\theta_i = 45°$ to $\theta_{eq} = 30°$; and a drop retracting from $\theta_i = 30°$ to $\theta_{eq} = 45°$. For each case, we consider two slip lengths, one large, $\lambda = 0.046875$, and one small, $\lambda = 0.01$ (the former value is chosen for convenience, since it is exactly 12 times the minimum cell size in the VoF simulations). These cases will be analyzed for both planar and axisymmetric drops. For the planar drops, the volume per unit length, i.e., area, is held constant at $A \approx 0.21$, while for the axisymmetric case the volume is held at $V \approx 0.15$, both corresponding to an initial front location $x_f = 0.6$ for $\theta_i = 45°$.

Figure 2 shows $\theta^3 - \theta^3_{eq}$ versus Ca for the planar drop. Both models show a similar trend. A transient initial period where Ca rapidly decreases while θ changes very little is reflected in the flat regions at the far right of each curve. This is followed by the spreading phase where θ relaxes to equilibrium and Ca is smaller than approximately 0.1. The most obvious difference between the curves resulting from the two models is that the L-W curves are generally shifted to the right (meaning, e.g., that for a given θ, the drops spread or retract faster under the L-W model). This shift can be traced back to the differences in the initial evolution of θ for the two models.

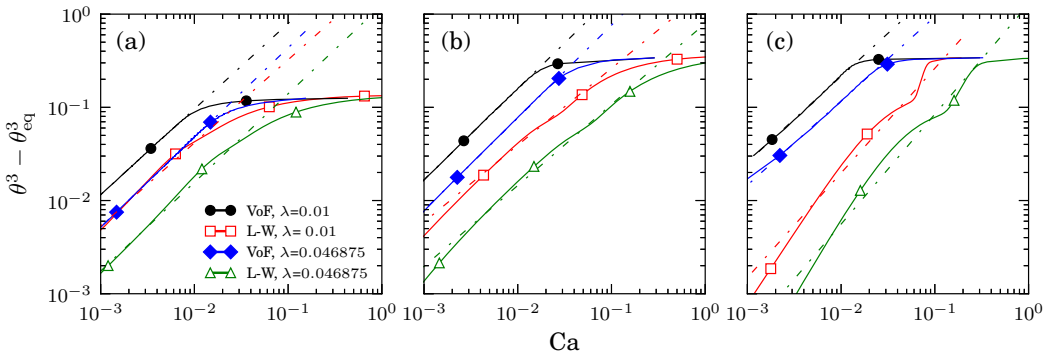

FIG. 2. Planar drop spreading and retracting for the L-W and VoF models for various slip lengths. The following cases were considered: (a) drop spreading from an initial contact angle of 30° to 15°; (b) drop spreading from 45° to 30°; (c) a drop retracting from 30° to 45°. The dashed lines show the best fits to the data of the form specified by Eq. (8). The definitions of the symbols used are given in the part (a) of this figure and that of Figures 4–6.

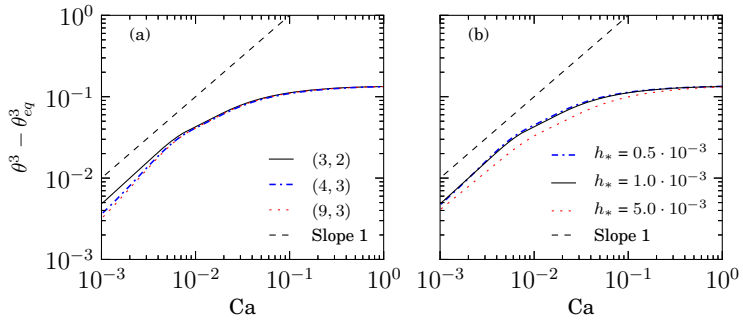

FIG. 3. Effects of h_* and the exponents (n, m) on the relation between Ca and θ for the planar (30°, 15°) spreading drop with $\lambda = 0.01$: (a) for different h_* and $(n, m) = (3, 2)$; (b) for different pairs (n, m) and $h_* = 10^{-3}$.

The dashed lines shown in Fig. 2 are the best fits of the functional form given by Eq. (8). The resulting exponent, β, is given in Table I; it turns out $0.9 < \beta < 1.0$ for the VoF model. For the L-W simulations, $\beta \approx 1$ for the $(\theta_i, \theta_{eq}) = (30°, 15°)$ and $\beta \lesssim 0.9$ for the (45°, 30°) spreading drop. For retracting drops, L-W results give $1.1 < \beta < 1.2$, but we also note that the retracting drop is not well described by the power law prescribed by Eq. (8).

There are two parameters in the L-W model that do not appear in VoF simulations, namely, the equilibrium thickness, h_*, and the pair of exponents (n, m). It is a natural question to ask whether these quantities influence the L-W results. Figure 3 shows that their influence is very weak. In particular, we see that values of h_* smaller than 10^{-3} do not affect the presented results; additional simulations (not shown for brevity) suggest that the exact value given to h_* is not relevant as long as $h_* \ll \lambda$. The influence of the exponents (n, m) is minor as well, although one may note that the pair (3, 2) gives the slope closer to unity for small Ca than the other two pairs of exponents.

Figure 4 shows $\theta^3 - \theta^3_{eq}$ versus Ca for an axisymmetric drop. The computed exponent, β, is given in Table II. Similarly to the planar case, we find that the power law behavior with $\beta = 1$ describes well the VoF simulations for spreading as well as for retracting drops, and the L-W simulations for spreading drops. For retracting drops, the L-W curves are not well described by the power law dependence prescribed by Eq. (8), viz. Fig. 4(c).

Remarks:

• It is appropriate to comment on the value of α in Eq. (8). Recall the rapid reduction in $\theta^3 - \theta^3_{eq}$ found in the L-W simulations for early times, see Fig. 1(a). This reduction, together with (approximate) power law behavior for late times ($\beta \approx 1$) requires that Ca is larger in the L-W model, for equivalent θ. In terms of Eq. (8), α must be smaller for L-W drops, so direct comparison of α

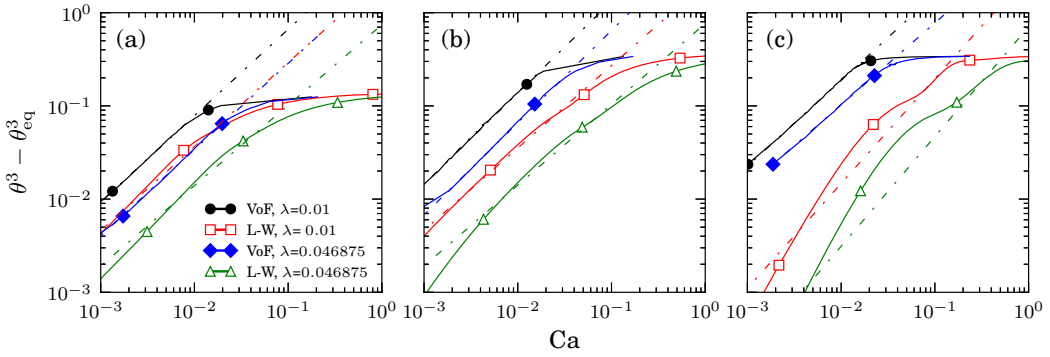

FIG. 4. Axisymmetric drop spreading and retracting for the L-W and VoF models for various slip lengths. The following cases were considered: (a) drop spreading from an initial contact angle of 30° to 15°; (b) drop spreading from 45° to 30°; (c) a drop retracting from 30° to 45°. The dashed line shows the best fits to the data of the form specified by Eq. (8).

TABLE II. Values of β resulting from fitting the evolution of axisymmetric drops with a spreading law of the form $\theta^3 - \theta_{eq}^3 \propto Ca^\beta$, for L-W and VoF simulations.

	VoF	L-W
30°–15°, slip 0.01	0.93	0.90
30°–15°, slip 0.046875	0.92	0.86
45°–30°, slip 0.01	0.98	0.88
45°–30°, slip 0.046875	0.99	0.87
30°–45°, slip 0.01	0.92	1.13
30°–45°, slip 0.046875	0.88	1.18

between the two models is not appropriate. This finding suggests that the interpretation of the length scales appearing in Eq. (7) has to be different; we further discuss these length scales below. Here we also note that the exact values of α are difficult to extract accurately from the present data, and this is one of the reason we have so far concentrated on β, which can be found much more accurately, and in addition is not influenced by the differences in the early time evolution.

• Recent works[8,34] consider the asymptotic limit of spreading drops in the small slip and contact angle limit, including discussion of the length scales entering into the C-V law, Eq. (7). The approach followed suggests that $h_c \propto x_f$ and $h_m \propto \lambda/\theta_{eq}$. As $\theta \to \theta_{eq} \ll 1$, volume conservation gives $x_f \propto \theta_{eq}^{-1/(d+2)}$ (where again $d = 0$, 1 for planar and axisymmetric geometry, respectively); from this one finds that $h_c/h_m \propto \theta_{eq}^{(d+1)/(d+2)}/\lambda$. We briefly discuss how our results compare to this prediction.

(i) Figures 2 and 4 show that increasing λ shifts both L-W and VoF curves downward a similar amount on the log-log plot, suggesting that both models share similar dependence on λ for both planar and axisymmetric drops, consistently with Ref. 34.

(ii) For both planar and axisymmetric drops, we observe in Figs. 2 and 4 that for spreading drops, the difference between the L-W and VoF curves increases for larger θ_{eq}. Careful inspection of the figures suggests that this increase is due to the fact that the VoF curves shift upwards as θ_{eq} is increased, while this shift (if any) is less pronounced for the L-W curves. The dependence of VoF results on θ_{eq} is consistent with Ref. 34.

(iii) Both models are more sensitive to variations of λ than to those of θ_{eq}, again consistently with the asymptotic results.[34]

A. Spreading of a perfectly wetting drop

We carry out here a second comparison between VoF and L-W simulations now for perfectly wetting drops (i.e., $\theta_{eq} = 0$). Under no-slip condition, the spreading drops are expected to follow an intermediate asymptotic behavior[35] for large t represented by a self-similar thickness profile whose contact line position, x_f, obeys the Tanner's law:[14]

$$x_f(t) = \xi_f t^\delta. \tag{9}$$

Here, ξ_f is a coefficient related to the thickness profile, and $\delta = 1/(7 + 3d)$, so that we have $\delta = 1/7$ for a planar drop, and $\delta = 1/10$ for an axisymmetric one.[36] When slip is included, the flow is no longer strictly self-similar due to the addition of this new length scale to the problem.[35] However, it has been shown that this effect is not strong if λ is much smaller than the average thickness of the drop, and a quasi self-similar solution can be obtained.[37] We will assume that this effect is negligible here at least for the time scales considered.

The simulations are performed using three different slip lengths ($\lambda = 0, 0.01, 0.046875$) for both planar and axisymmetric drops. Here, we consider $\lambda = 0$ in addition to non-zero values so to be able to see clearly the influence of λ on reaching the asymptotic regime described above. Considering $\lambda = 0$ requires few adjustments in our computations which we now briefly describe. In the L-W model, we simply put $\lambda = 0$ in Eq. (4). Now the only additional length scale introduced in the

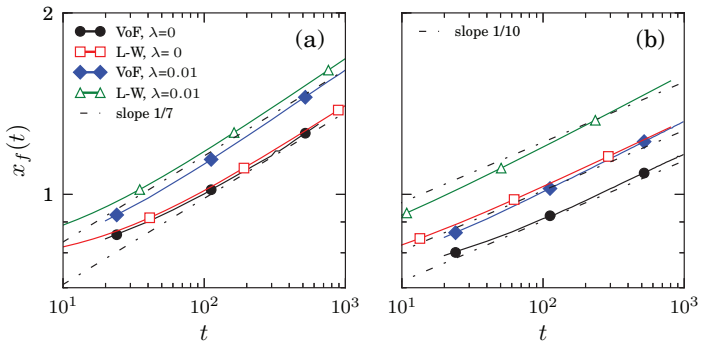

FIG. 5. Front location as a function of time, $x_f(t)$, for a perfectly wetting drop ($\theta_{eq} = 0$) in L-W and VoF simulations: (a) planar case; (b) axisymmetric case. The dashed lines show the exponent, δ, predicted by Tanner's law for each case.

problem is h_*; the results (weakly) depend on this quantity, as discussed in some details in an earlier work.[38] In VoF simulations, a numerical slip of the order of the mesh size is always present, leading to a mesh-size prewetting layer ahead of the contact line when $\theta_{eq} = 0$. Clearly, this computational feature suggests that one may expect an influence of the numerical resolution on the results;[39] to optimize the computational cost, we limit the minimum mesh size to $1/2^8$ units. At this resolution, the effect of the mesh is found to be negligible on the results we present below. For the remainder of this section, we will calculate the front location for VoF droplets as the point of inflection of the fluid profile, rather than as the intersection of the reconstructed interface with the substrate.

Similarly to the calculations carried out for non-zero θ_{eq}, we start with drops of a given initial contact angle, θ_i, and let the drops spread freely. Figure 5 shows the front location as a function of time, $x_f(t)$. For clarity, we show in this figure the results for $\lambda = 0$, 0.01 only. Dashed lines show profiles proportional to $t^{1/7}$ (Fig. 5(a)) and $t^{1/10}$ (Fig. 5(b)); the behavior of no-slip simulations is seen to agree with these powers reasonably well for large times. To go beyond visual comparison, we compute the value of δ in Eq. (9) from both models by a least squares fitting over a range of times when δ is approximately constant. Table III shows the values of δ obtained. The L-W and VoF calculations yield similar exponents for all slip lengths considered, and both show that δ decreases for smaller λ, approaching the asymptotic values.

IV. COLLAPSE OF LIQUID RINGS

As a final comparison, we consider the problem of a collapsing ring, motivated by our desire to consider a geometry that is more complex than the one of a drop, but that still allows for identifying clearly the differences between the models. In addition, we will use this problem to more explicitly demonstrate the influence of slip on the dynamics.

TABLE III. Exponents for the power law of the front position, $x_f(t)$, in the perfectly wetting case ($\theta_{eq} = 0$). The results are given in fractional form to help comparison with Tanner's law exponent δ, 1/7 and 1/10, for the planar and axisymmetric cases, respectively.

Case	δ_{VoF}	δ_{L-W}
Planar, slip 0.046875	1/6.0	1/6.0
Planar, slip 0.01	1/6.3	1/6.2
Planar, no-slip	1/6.2	1/6.6
Axisymmetric, slip 0.046875	1/7.2	1/7.7
Axisymmetric, slip 0.01	1/8.5	1/8.1
Axisymmetric, no-slip	1/9.4	1/9.0

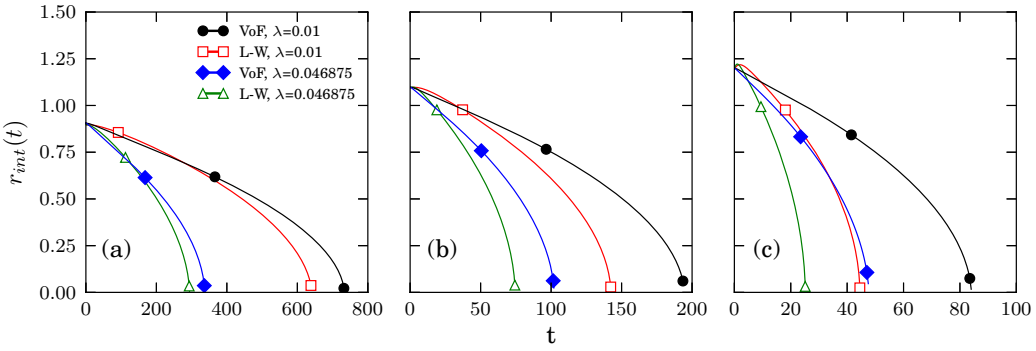

FIG. 6. Inner radius, $r_{int}(t)$, for L-W and VoF simulations of a collapsing ring: (a) $\theta_{eq} = 15°$; (b) $\theta_{eq} = 30°$; (c) $\theta_{eq} = 45°$.

The ring is defined by its internal and external radii, r_{int} and r_{ext}, respectively, as well as by the radius, R, of its circular cross section. Thus, the liquid is initially inside the region described by

$$0 \le y \le -R\cos\theta + \sqrt{R^2 - (r - r_0)^2}, \tag{10}$$

where $r_0 = (r_{ext} + r_{int})/2$ is the mean radius, $r^2 = x^2 + z^2$ with $r_{int}\cos\phi \le x \le r_{ext}\cos\phi$ and $r_{int}\sin\phi \le y \le r_{ext}\sin\phi$ $(0 < \phi < 2\pi)$, and θ is the contact angle.

The radius, R, is chosen to be the same as that in previously considered axisymmetric drops ($R \approx 3.5$, 1.4, 0.8, for $\theta_{eq} = 15°$, 30°, and 45°, respectively), and the mean radius, r_0, is held constant at $r_0 = 1.8$. In our setup, we consider rings with equal initial contact angles, θ_i, at the internal and external radii, and both equal to the equilibrium angle for static axisymmetric drops, θ_{eq}. However, the ring is not in equilibrium since the curvatures, $1/r_{int}$ and $1/r_{ext}$, yield different capillary pressures which cannot be balanced by the same contact angle.[18] Consequently, the ring develops an inward flow which eventually leads to a collapse into a single central axisymmetric drop. In the present work, we assume azimuthal symmetry and do not consider fully three-dimensional features of the dynamics, which may lead to instabilities and breakup.[18]

Figure 6 shows the time evolution of the inner radius of the ring for both VoF and L-W simulations. In particular, we will be interested in the time, τ, the collapse takes, defined as the time when the interior radius vanishes. Table IV shows the resulting values of τ, together with the ratio between the results of the two models. We note that this ratio decreases for smaller θ_{eq}, suggesting that the both models predict increasingly similar dynamics for small contact angles. For large θ_{eq} there are, however, significant differences, as can be seen explicitly in Figs. 6(a)–6(c). We point out that these differences in dynamics cannot be predicted based simply on the thickness profiles. To illustrate this point, Fig. 7 shows the profiles resulting from the two models at the times when the inner ring radii are at the same location (Figs. 7(a) and 7(b)), in addition to the equilibrium (long-time) result (Fig. 7(c)). We see that the corresponding shapes barely differ, but still lead to considerably different dynamics.

TABLE IV. Ring collapse times, τ_{VoF} and τ_{L-W}, and their ratio, τ_{VoF}/τ_{L-W}. The first column specifies the equilibrium contact angle, θ_{eq}, and the slip length, λ.

Case	τ_{VoF}	τ_{L-W}	τ_{VoF}/τ_{L-W}
15°, slip 0.01	733	641	1.1
15°, slip 0.046875	337	294	1.1
30°, slip 0.01	194	142	1.4
30°, slip 0.046875	102	74	1.4
45°, slip 0.01	84	44	1.9
45°, slip 0.046875	48	25	1.9

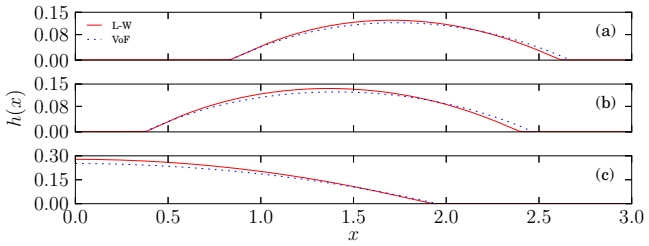

FIG. 7. Ring profiles resulting from VoF and L-W simulations. (a) and (b) show the profiles at the times when the inner radii are at the same location for both models, and (c) shows the equilibrium solution.

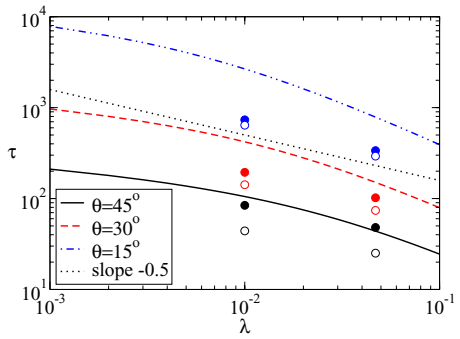

FIG. 8. Collapse times, τ, of rings. Solid, dashed, and dash-dotted lines show the inverse of the growth rate, ω_0, of the azimuthally symmetric mode obtained from the linear stability analysis; filled/hollow circles show τ_{VoF} and τ_{L-W}, respectively.

Regarding the influence of slip length, note that Fig. 6 shows that a smaller λ leads to a larger collapse time, with slip playing a similar role in both models. Additional more precise observations can be made: for both VoF and L-W simulations, τ approximately halves when λ increases by a factor close to four, viz. Table IV. This would suggest that a dependence $\tau \sim \lambda^{-0.5}$ could be expected (see dashed line in Fig. 8). In fact, a similar behavior is obtained when we consider the linear stability analysis (LSA) of a contracting ring within L-W approach,[18] by recalling that the collapse time, τ, can be related to the inverse of the growth rate for the azimuthally symmetric mode, ω_0. Figure 8 shows that the LSA predicts a dependence of τ on λ that is not too far from what is found in simulations. The overestimate of τ computed using the LSA is as expected, since the presented estimate is based on the value of ω_0 computed at $t = 0$ and therefore does not include an increase of collapse speed as the ring decreases in size.

V. CONCLUSIONS

In this work, we report on comparison between direct solutions of Navier-Stokes equations computed using a volume-of-fluid method, and the long-wave based simulations. We consider two simple geometries, drops and rings, with the goal of avoiding complexities that are associated with more complicated geometries. To further facilitate the comparison, we consider the flow regime characterized by low Reynolds and capillary numbers, where L-W theory is expected to apply, and implement Navier slip condition in both models with the same goal.

For partially wetting drops, characterized by non-zero equilibrium contact angle, θ_{eq}, the comparison is carried out by considering consistency with the asymptotic C-V law. While in general our findings are as expected – that L-W theory agrees well with the VoF results and the C-V law for small θ_{eq} – we also uncover additional features of the results, summarized here: (i) the deviations of L-W results from the behavior expected based on the C-V law and VoF simulations is particularly strong for retracting drops, and in azimuthal geometry; (ii) the initial stages of spreading or retracting differ significantly between the models, for all considered θ_{eq}; (iii) the degree of agreement between the two models is not influenced by the values assigned to the slip length, λ—in other words, slip

influences both models in a similar manner. To our knowledge, these findings have not been reported in the literature.

For perfectly wetting drops, with $\theta_{eq} = 0$, both models are found to agree well with the predictions of Tanner's law in the case of no-slip. Non-zero slip length modifies the results and introduces deviations from Tanner's law as expected; an important finding here is that the two models agree well with each other for non-vanishing slip.

When the two models are applied to collapse of a liquid ring, the results are found to be in good agreement for small θ_{eq}, while for larger θ_{eq}, the collapse time under L-W simulations is as much as twice as fast relative to the one found using VoF simulations. Again, the slip length has little effect on the degree of comparison of the two models.

While in the present work we have considered only a classical L-W formulation, it would be of interest to explore whether the recently proposed improvements of this formulation (see, e.g., Ref. 40), lead to significant differences; in addition, one wonders what is the influence of the uncovered differences when more complex evolution is expected, such as in the problems where various types of instabilities are relevant. These questions will be considered in our future work.

ACKNOWLEDGMENTS

This research was partly supported by NSF Grant Nos. DMS-1320037 (S.A.) and CBET-1235710 (L.K.) and by Consejo Nacional de Investigaciones Cientificas y Tecnicas (CONICET, Argentina) Grant No. PIP 844/2011 (J.D.). The authors acknowledge many useful discussions with J. Fowlkes, A. González, and P. Rack.

APPENDIX A: NAVIER-STOKES SIMULATIONS

What follows, unless otherwise specified, is an overview of the method given in Ref. 26. Spatial discretization is accomplished through a quad-tree in two dimensions; the domain is decomposed into discrete square volumes, referred to as cells. All variables are defined at cell centers, and are interpreted as their average over the cell. This mesh is adaptive, allowing to effectively treat regions of very different interface curvatures and spatial scales. The interface between the two fluids is tracked using an implementation of the VoF method. The VoF method tracks the interface by introducing a volume fraction function, T, which is equal to the fraction of the cell occupied by the fluid phase. The volume fraction is advected with the fluid flow, obeying the transport equation:

$$\frac{\partial T}{\partial t} + \nabla \cdot (\mathbf{u}T) = 0\,.$$

The interface in a cell is reconstructed as the linear function of the position x: $\mathbf{m} \cdot \mathbf{x} = \alpha$, where $\mathbf{m}$ is the interface normal computed as ∇T by a finite difference stencil. The right-hand side α is solved for using the normal and volume fraction (see Ref. 41).

The solution of the N-S equations is accomplished through a time-splitting projection method. First, a predictor step calculates the auxiliary velocity field $\mathbf{u}_*$ by applying the advection terms and viscous forcing (note that in what follows a subscripted asterisk will indicate that the term is evaluated on the auxiliary field):

$$\rho_{n+1/2}\left[\frac{\mathbf{u}_* - \mathbf{u}_n}{\Delta t} + \mathbf{u}_{n+1/2} \cdot \nabla \mathbf{u}_{n+1/2}\right] = \nabla \cdot [2\mu_{n+1/2}((1-\eta)D_n + \eta D_*)]\,, \tag{A1}$$

where $D = \frac{1}{2}(\nabla \mathbf{u} + \nabla \mathbf{u}^T)$ is the rate of deformation tensor. The parameter η characterizes the implicitness of the method; $\eta = 1/2$ yields a Crank-Nicholson, second order scheme, and $\eta = 1$ yields first-order accurate, fully implicit scheme. The time step is variable, and the explicit treatment of the surface tension requires[26] that the time step satisfies $\Delta t \leq \sqrt{\rho \Delta^3/(\pi\sigma)}$, where Δ is the width of the smallest computational cell. In our surface tension driven flows, this constraint dominates the time-stepping restrictions. The advection term $\mathbf{u}_{n+1/2} \cdot \nabla \mathbf{u}_{n+1/2}$ is estimated using a conservative Godunov method proposed in Ref. 42. The discrete equation is solved using a multigrid method with Jacobi iteration scheme.

The surface tension is added to $\mathbf{u}_*$ in the next step, and is computed as a modification of the continuum surface force implementation of the surface tension proposed in Ref. 25, where ∇T is used to approximate the $\delta_s \mathbf{n}$ in Eq. (1):

$$\mathbf{u}_* \leftarrow \mathbf{u}_* + \frac{\Delta t \sigma \kappa_{n+1/2}}{\rho_{n+1/2}} \nabla T_{n+1/2} \,. \tag{A2}$$

Interface curvature, κ, is estimated using a modification of the height function method[43–45] first proposed in Ref. 46 and described in detail in Ref. 26. In this method, the "height" of the fluid interface in a computational cell is calculated above a reference axis (e.g., the x axis). If we refer to the height function as f, then the curvature of the interface in two dimensions is given by the standard formula $\kappa = f''/(1 + f'^2)^{3/2}$, so that three fluid heights are required for a finite difference approximation of this curvature in each cell. The height functions are also used to impose the contact angle, as described below.

Since the velocity field must be incompressible, the auxiliary field is written, using the Helmholtz decomposition, as

$$\mathbf{u}_* = \mathbf{u}_{n+1} + \frac{\Delta t}{\rho_{n+1/2}} \nabla p_{n+1/2} \,, \tag{A3}$$

where again p is the pressure. Taking the divergence of both sides leads to a Poisson equation:

$$\nabla \cdot \left(\frac{\Delta t}{\rho_{n+1/2}} \nabla p_{n+1/2} \right) = \nabla \cdot \mathbf{u}_* \,. \tag{A4}$$

The divergence-free velocity field is finally given by

$$\mathbf{u}_{n+1} = \mathbf{u}_* - \frac{\Delta t}{\rho_{n+1/2}} \nabla p_{n+1/2}. \tag{A5}$$

The volume fraction T is solved for at half timesteps by a conservative method; the variables $\mu_{n+1/2}$ and $\rho_{n+1/2}$ are thus known through their functional dependence on the volume fraction function.

Finally, the contact angle in the VoF code is implemented as described in Ref. 44. In this method, the slope of the interface in the contact line cell is imposed so that the angle formed by the interface with the substrate is θ_{eq}, and the forcing due to the contact angle enters into Eq. (1) through the surface tension term. It is thus sufficient to modify the computation of the curvature term to take this into account. The height of the fluid in the contact line cell is found from a linear reconstruction of the interface in that cell, using the value of the volume fraction T and the slope determined by θ_{eq}. In order to have a large enough stencil of heights to compute the curvature, "ghost cells" are introduced, which are cells outside the domain where the height function and T are defined. The height function in the ghost cells is found by extending the linear reconstruction in the contact line cell into the ghost cells. The same method as above is used for $\theta_{eq} = 0$, and is equivalent to setting $T = 1$ in the ghost cells.

APPENDIX B: NUMERICAL VALIDATION

In our VoF simulations, the solution was calculated on an adaptive mesh refined on the drop surface to a resolution of $\Delta = 1/2^8$, while parts of the domain far from the surface were refined to $1/2^4$. To test the convergence of the method, we present the case when the planar drop spreads from $\theta_i = 30^\circ$ to $\theta_{eq} = 15^\circ$. The average relative difference is calculated as

$$\mathrm{Avg}_\Delta = \frac{1}{t_{max}} \int_0^{t_{max}} \frac{|x_f(t) - x_{ref}(t)|}{x_{ref}(t)} dt \,,$$

where x_{ref} is the drop radius computed with $\Delta = 1/2^8$, and x_f is computed with $\Delta = 1/2^5$, $1/2^6$, and $1/2^7$. We restrict our attention to a representative portion of the drop spreading, so that t_{max} is the time it takes for the drop radius to be within 1% of its equilibrium value, as computed using $\Delta = 1/2^8$. Figure 9 plots Avg_Δ and shows that mesh effects are negligible when compared to the drop radius.

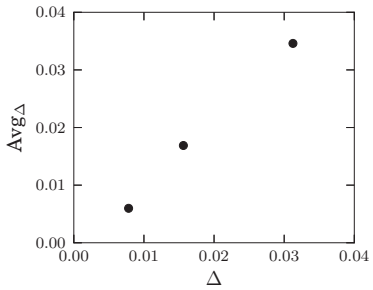

FIG. 9. Relative error for planar spreading drop. The error is computed as the average relative difference between the front location compared to the one found using $\Delta = 1/2^8$.

Hocking and Rivers[21] derived an asymptotic solution for the radius of a spreading drop. In their derivation, the flow is governed by the Stokes equations, and the effects of gravity are ignored. Additionally, the condition on the solid substrate is assumed to be the Navier slip condition (see Eq. (3)), where the slip length is taken to be small relative to the drop size. No limitations on the contact angle are imposed. Their solution yields the following ordinary different equation (ODE) for the drop radius, x_f

$$2\frac{dx_{f_a}}{dt} = \frac{G(\theta) - G(\theta_{eq})}{\ln(x_f) - \ln(\lambda) - Q_O(\theta) + Q_i(\theta_{eq})}, \tag{B1}$$

where

$$G(\theta) = \int_0^\theta \frac{\vartheta - \sin\vartheta\cos\vartheta}{\sin\vartheta} d\vartheta .$$

The functions Q_O and Q_i were computed by interpolating Table 1 in Ref. 21. The contact angle, θ, is related to the drop volume and front location through conservation of volume, so that Eq. (B1) can be solved using standard ODE solvers.

We present the case of the axisymmetric drop spreading from 45° to 30°. In order for Eq. (B1) to apply, the denominator must be greater than 0, so for our parameters we find the condition that $\lambda \lesssim 0.03$. We thus choose $\lambda = (0.028, 0.016, 0.008, 0.004)$. The drop radius was computed using the VoF solver, $x_{f_{VoF}}$, and the asymptotic solution, x_{f_a}, for each slip length. The average relative difference between numerical and asymptotic solution was computed by the integration

$$\text{Avg}\frac{|x_{f_{VoF}} - x_{f_a}|}{x_{f_{VoF}}} = \frac{1}{t_{max}}\int_0^{t_{max}} \frac{|x_{f_{VoF}} - x_{f_a}|}{x_{f_{VoF}}} dt ,$$

where t_{max} is again chosen so that $x_{f_{VoF}}$ is within 1% of its equilibrium value. Note that the time it takes for the VoF solution to reach equilibrium is λ-dependent, so that the comparison is carried out over appropriate ranges for each λ considered.

Figure 10(a) shows the relative difference between the two results. We see that the front locations agree well in the limit of small λ. Another comparison that can be carried out involves considering the difference in the time scales. We compute the spread times as the time it takes the VoF solution and the asymptotic solution to reach 1% of the respective equilibrium values; denote these τ_{VoF} and τ_a. The relative difference between the two is computed as $|\tau_{VoF} - \tau_a|/\tau_{VoF}$. Figure 10(b) shows the relative difference of the spread times. For larger λ, the asymptotic solution predicts that a drop spreads much faster, compared to the simulation results. However, for small λ, the difference in spreading times is less than 10% of τ_{VoF}, and on average the relative difference in the computed front locations is of the order of 10^{-3}.

To conclude, we find that the results of the simulations are fully converged for the grid resolutions implemented. Furthermore, the location of the front as a function of time agrees very well with existing asymptotic results for a spreading drop. The VoF based solver thus allows for accurate simulations of contact angle driven spreading phenomena.

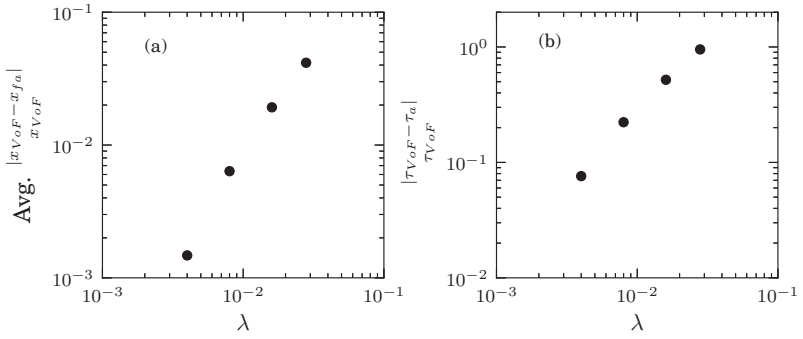

FIG. 10. Comparison of VoF simulations with asymptotic solution[21] for a drop spreading from 30° to 15° as a function of the slip length: (a) the average relative difference between the front locations; (b) the relative difference in spread times.

[1] R. Cox, "The dynamics of the spreading of liquids on a solid surface. Part 1. Viscous flow," J. Fluid Mech. **168**, 169 (1986).
[2] Y. Shikhmurzaev, "Moving contact lines in liquid/liquid/solid systems," J. Fluid Mech. **334**, 211 (1997).
[3] P. D. Spelt, "A level-set approach for simulations of flows with multiple moving contact lines with hysteresis," J. Comput. Phys. **207**, 389 (2005).
[4] S. Afkhami, S. Zaleski, and M. Bussmann, "A mesh-dependent model for applying dynamic contact angles to VOF simulations," J. Comput. Phys. **228**, 5370 (2009).
[5] J. E. Sprittles and Y. D. Shikhmurzaev, "Finite element framework for describing dynamic wetting phenomena," Int. J. Numer. Methods Fluids **68**, 1257 (2012).
[6] M. Sussman, "A method for overcoming the surface tension time step constraint in multiphase flows II," Int. J. Numer. Methods Fluids **68**, 1343 (2012).
[7] Y. Sui and P. D. Spelt, "An efficient computational model for macroscale simulations of moving contact lines," J. Comput. Phys. **242**, 37 (2013).
[8] D. Bonn, J. Eggers, J. Indekeu, J. Meunier, and E. Rolley, "Wetting and spreading," Rev. Mod. Phys. **81**, 739 (2009).
[9] A. Oron, S. H. Davis, and S. G. Bankoff, "Long-scale evolution of thin liquid films," Rev. Mod. Phys. **69**, 931 (1997).
[10] R. V. Craster and O. K. Matar, "Dynamics and stability of thin liquid films," Rev. Mod. Phys. **81**, 1131 (2009).
[11] R. Goodwin and G. M. Homsy, "Viscous flow down a slope in the vicinity of a contact line," Phys. Fluids A **3**, 515 (1991).
[12] J. Fowlkes, L. Kondic, J. Diez, Y. Wu, and P. Rack, "Self-assembly versus directed assembly of nanoparticles via pulsed laser induced dewetting of patterned metal films," Nano Lett. **11**, 2478 (2011).
[13] O. Voinov, "Hydrodynamics of wetting," Fluid Dyn. **11**, 714 (1976).
[14] L. Tanner, "Spreading of silicone oil drops on horizontal surfaces," J. Phys. D **12**, 1473 (1979).
[15] Y. Wu, J. Fowlkes, P. Rack, J. Diez, and L. Kondic, "On the breakup of patterned nanoscale copper rings into droplets via pulsed-laser-induced dewetting: competing liquid-phase instability and transport mechanisms," Langmuir **26**, 11972 (2010).
[16] Y. Wu, J. Fowlkes, N. Roberts, J. Diez, L. Kondic, A. González, and P. Rack, "Competing liquid phase instabilities during pulsed laser induced self-assembly of copper rings into ordered nanoparticle arrays on SiO_2," Langmuir **27**, 13314 (2011).
[17] S. Afkhami and L. Kondic, "Numerical simulation of ejected molten metal nanoparticles liquified by laser irradiation: Interplay of geometry and dewetting," Phys. Rev. Lett. **111**, 034501 (2013).
[18] A. G. González, J. A. Diez, and L. Kondic, "Stability of a liquid ring on a substrate," J. Fluid Mech. **718**, 246 (2013).
[19] E. B. Dussan V, "The moving contact line: the slip boundary condition," J. Fluid Mech. **77**, 665 (1976).
[20] H. P. Greenspan, "On the motion of a small viscous droplet that wets a surface," J. Fluid Mech. **84**, 125 (1978).
[21] L. Hocking and A. Rivers, "The spreading of a drop by capillary action," J. Fluid Mech. **121**, 425 (1982).
[22] P. J. Haley and M. J. Miksis, "The effect of the contact line on droplet spreading," J. Fluid Mech. **223**, 57 (1991).
[23] C. Huh and L. E. Scriven, "Hydrodynamic model of steady movement of a solid/liquid/fluid contact line," J. Colloid Interface Sci. **35**, 85 (1971).
[24] J. Diez and L. Kondic, "On the breakup of fluid films of finite and infinite extent," Phys. Fluids **19**, 072107 (2007).
[25] J. Brackbill, D. Kothe, and C. Zemach, "A continuum method for modeling surface tension," J. Comput. Phys. **100**, 335 (1992).
[26] S. Popinet, "An accurate adaptive solver for surface-tension-driven interfacial flows," J. Comput. Phys. **228**, 5838 (2009).
[27] S. Popinet, "The Gerris flow solver," http://gfs.sourceforge.net/ (2012), Version 1.3.2.
[28] C. A. Perazzo and J. Gratton, "Navier-Stokes solutions for parallel flow in rivulets on an inclined plane," J. Fluid Mech. **507**, 367 (2004).
[29] J. N. Israelachvili, *Intermolecular and Surface Forces*, 2nd ed. (Academic Press, New York, 1992).
[30] L. Schwartz and R. Eley, "Simulation of droplet motion on low-energy and heterogeneous surfaces," J. Colloid Interface Sci. **202**, 173 (1998).
[31] A. Münch and B. Wagner, "Contact-line instability of dewetting thin films," Physica D **209**, 178 (2005).
[32] J. M. Gomba and G. M. Homsy, "Analytical solutions for partially wetting two-dimensional droplets," Langmuir **25**, 5684 (2009).
[33] J. Diez and L. Kondic, "Computing three-dimensional thin film flows including contact lines," J. Comput. Phys. **183**, 274 (2002).

[34] J. Eggers, "Toward a description of contact line motion at higher capillary numbers," Phys. Fluids **16**, 3491 (2004).
[35] G. Barenblatt, *Scaling, Self-Similarity, and Intermediate Asymptotics* (Cambridge University Press, New York, 1996).
[36] J. Diez, R. Gratton, L. Thomas, and B. Marino, "Laplace pressure driven drop spreading," Phys. Fluids **6**, 24 (1994).
[37] R. Gratton, J. A. Diez, L. P. Thomas, B. Marino, and S. Betelú, "Quasi-self-similarity for wetting drops," Phys. Rev. E **53**, 3563 (1996).
[38] J. Diez, L. Kondic, and A. L. Bertozzi, "Global models for moving contact lines," Phys. Rev. E **63**, 011208 (2000).
[39] M. Renardy, Y. Renardy, and J. Li, "Numerical simulation of moving contact line problems using a volume-of-fluid method," J. Comput. Phys. **171**, 243 (2001).
[40] J. Snoeijer, "Free-surface flows with large slope: beyond lubrication theory," Phys. Fluids **18**, 021701 (2006).
[41] R. Scardovelli and S. Zaleski, "Analytical relations connecting linear interfaces and volume fractions in rectangular grids," J. Comput. Phys. **164**, 228 (2000).
[42] J. Bell, P. Colella, and H. Glaz, "A second-order projection method for the incompressible Navier-Stokes equations," J. Comput. Phys. **85**, 257 (1989).
[43] M. Francois, S. Cummins, E. Dendy, D. Kothe, J. Sicilian, and M. Williams, "A balanced-force algorithm for continuous and sharp interfacial surface tension models within a volume tracking framework," J. Comput. Phys. **213**, 141 (2006).
[44] S. Afkhami and M. Bussmann, "Height functions for applying contact angles to 2D VOF simulations," Int. J. Numer. Methods Fluids **57**, 453 (2008).
[45] M. Sussman, "A second order coupled level set and volume-of-fluid method for computing growth and collapse of vapor bubbles," J. Comput. Phys. **187**, 110 (2003).
[46] M. Torrey, L. Cloutman, R. Mjolsness, and C. Hirt, "NASA-VOF2D: a computer program for incompressible flows with free surfaces," NASA STI/Recon Technical Report N (1985), Vol. 86, p. 30116.